Geochimica et Cosmochimica Acta 349 (2023) 115–125

Contents lists available at ScienceDirect

Geochimica et Cosmochimica Acta

journal homepage: www.elsevier.com/locate/gca

Structural incorporation of iron influences biomethylation potential of mercury sulfide

Yunyun Ji [a,1], Shan Gao [b,1], Rui Si [c], Zhanhua Zhang [a], Li Tian [a,d], Wenyu Guan [a], Weichao Wang [b], Jiubin Chen [e], Wei Chen [a], Pedro J.J. Alvarez [f], Tong Zhang [a,*]

[a] College of Environmental Science and Engineering, Ministry of Education Key Laboratory of Pollution Processes and Environmental Criteria, Tianjin Key Laboratory of Environmental Remediation and Pollution Control, Nankai University, 38 Tongyan Rd., Tianjin 300350, China
[b] College of Electronic Information and Optical Engineering, Nankai University, 38 Tongyan Rd., Tianjin 300350, China
[c] Shanghai Synchrotron Radiation Facility, Shanghai Institute of Applied Physics, Chinese Academy of Sciences, 239 Zhangheng Rd., Shanghai 201204, China
[d] School of Resource and Environmental Engineering, Jiangxi University of Science and Technology, 156 Hakka Ave., Ganzhou 341000, China
[e] School of Earth System Science, Tianjin University, 92 Weijin Rd., Tianjin 300072, China
[f] Department of Civil and Environmental Engineering, Rice University, 6100 Main Street, Houston, TX 77005, United States

ARTICLE INFO

Article history:
Received 30 November 2022
Accepted 31 March 2023
Available online 5 April 2023
Associate editor: Elizabeth Herndon

Keywords:
Mercury biogeochemistry
Methylmercury
Microbial methylation
Nanoparticle
Ferrous iron

ABSTRACT

Mercury and ferrous iron commonly co-exist in anaerobic environments, the hotspots of microbial mercury methylation that leads to formation of neurotoxic methylmercury. However, the influence of ferrous iron on mercury bioavailability and methylation remains unclear. Here, we discover that microbial methylmercury production is inhibited by iron addition in a non-monotonical manner, reaching the minimal level at the initial molar ratio of dissolved Fe/Hg as 1/3, when highly aggregated Hg–S–Fe nanoparticles occur and prevent the nanoparticle–bacteria interactions. The dominant mercury species formed upon Hg–S–Fe co-precipitation is iron-incorporated nano-metacinnabar with short-range structural disorder. The methylation potential of this mercury species is inversely correlated with the aggregation state of nanoparticles. The non-monotonical trends of the aggregation state and subsequent methylation of nano-metacinnabar are due to the opposite effects of ferrous iron on the nucleation and particle attachment that determine the formation of nanoparticle aggregates. Increased Fe/Hg ratio hinders particle nucleation and thus decreases the density of particle monomers for aggregation. However, Fe substitution of sub-surface Hg weakens the inner-sphere coordination of surface Hg with natural thiol ligands and consequently enhances nano-metacinnabar aggregation. This new mechanistic insight is important for assessing and minimizing the risks of mercury methylation, and informs how intertwined iron and sulfur cycling may influence metal bioavailability in the changing environment.

© 2023 Elsevier Ltd. All rights reserved.

1. Introduction

Inorganic mercury is released to the environment from various natural and anthropogenic sources, such as volcanic eruption, gold mining and fossil fuel combustion (United Nations Environment Programme, 2019). Of particular concern is the conversion of inorganic mercury to the bioaccumulative neurotoxin, methylmercury (MeHg), which biomagnifies through the food chain and severely endangers human health (Driscoll et al., 2013; Tang et al., 2020). Mercury methylation is predominantly driven by anaerobic microorganisms carrying *hgcAB* genes dwelling in aquatic settings, such as sulfate reducing bacteria, iron reducing bacteria, and methanogens (Parks et al., 2013; Podar et al., 2015). Given that sulfate reduction and iron reduction are common electron-accepting processes in anaerobic environments (Muyzer and Stams, 2008; Lovley, 1991), the main metabolic products from these processes, sulfide and ferrous iron, are expected to co-occur with mercury at the environmental "hotspots" for MeHg production.

The environmental significance of understanding the influence of sulfide and iron on mercury bioavailability and methylation has long been recognized, but findings from previous research were inconsistent (Mehrotra et al., 2003; Mehrotra and Sedlak, 2005; Han et al., 2008; Ulrich and Sedlak, 2010; Bravo et al., 2015). On one hand, substantial mercury methylation was observed in iron-rich sediments impacted by organic matter discharged from sewage treatment plants (Bravo et al., 2015). Upon

* Corresponding author.
E-mail address: zhangtong@nankai.edu.cn (T. Zhang).
[1] These authors contributed equally to this work.

https://doi.org/10.1016/j.gca.2023.03.035
0016-7037/© 2023 Elsevier Ltd. All rights reserved.

addition of relatively low concentration of iron, MeHg production was unchanged or mildly enhanced in sediment slurries (Mehrotra and Sedlak, 2005; Han et al., 2008). On the other hand, iron amendment was reported to mitigate MeHg production in pure cultures of methylating bacteria and anoxic sediments (Mehrotra et al., 2003; Ulrich and Sedlak, 2010). These mitigating effects have been explained by two mechanisms related to how ferrous iron modulates the abundance and speciation of dissolved mercury, including mercury sequestration via precipitation with (Jeong et al., 2007; Jeong et al., 2010; Skyllberg and Drott, 2010; Zhang et al., 2014; Rivera et al., 2019) or adsorption to iron sulfide (Merritt and Amirbahman, 2007; Jeong et al., 2007; Jeong et al., 2010; Rivera et al., 2019), as well as iron decreasing the concentration of dissolved sulfide that reduces the formation of dissolved neutral mercury sulfide complexes (Mehrotra et al., 2003; Ulrich and Sedlak, 2010).

Improved understanding of mercury bioavailability requires not only attention to dissolved mercury speciation at equilibrium conditions (Benoit et al., 1999), but also consideration of kinetically-controlled metastable species of particulate mercury (Gerbig et al., 2011; Zhang et al., 2012). In fact, previous research has shown that nanoparticulate mercury is widely present in the environment and appears to be persistent (Poulin et al., 2016; Gilmour et al., 2018; Xu et al., 2021), as the precipitation processes of mercury sulfide are kinetically hindered by natural organic matter (NOM) and low-molecular-weight thiols (Deonarine and Hsu-Kim, 2009; Poulin et al., 2017; Mazrui et al., 2018). Although nanoparticulate mercury led to prominent MeHg production in a number of pure culture (Zhang et al., 2012; Graham et al., 2012; Graham et al., 2013; Tian et al., 2021), sediment microcosm (Jonsson et al., 2012; Zhang et al., 2014; Mazrui et al., 2016; Ndu et al., 2018) and mesocosm studies (Jonsson et al., 2014), the effects of iron on the formation and bioavailability of nanoparticulate mercury remains unclear and nanoparticulate mercury–sulfide–iron (Hg–S–Fe) species has not yet been proposed, which may help understand the wide range of mercury methylation potential observed in natural environment (Cossa et al., 2014; Tang et al., 2020). Here, we discern the nature of the precipitation products in the Hg–S–Fe system, and the mechanisms via which ferrous iron modulates the nano-crystalline structure and subsequent methylation potential of agglomerated nanoparticulate mercury.

2. Materials and methods

2.1. Co-precipitation of Hg–S–Fe in the presence of natural ligands

Ultrapure water (>18.0 MΩ·cm) was purged with high purity nitrogen (99.999%) prior to use in all anaerobic experiments. Sodium nitrate ($NaNO_3$, 99.0%) and sodium sulfide nonahydrate ($Na_2S{\cdot}9H_2O$, 99.99%) were purchased from Aladdin Bio-Chem Technology Co., Ltd. (Shanghai, China). Ferrous sulfate heptahydrate ($FeSO_4{\cdot}7H_2O$, >99%) was purchased from Dalian Meilun Biotechnology Co., Ltd. (Dalian, China). Mercury nitrate monohydrate ($Hg(NO_3)_2{\cdot}H_2O$, analytical grade) was purchased from Sinopharm Chemical Reagent Co., Ltd. (Shanghai, China) and used to prepare the mercury (Hg) stock solution containing 0.15 M HNO_3 (trace metal grade). Reduced glutathione (GSH, 99%) was purchased from Macklin Biochemical Co., Ltd. (Shanghai, China). The stock solutions of Na_2S, $FeSO_4$ and GSH were prepared using N_2-purged ultrapure water within 4 h before the precipitation experiments. Suwannee River Fulvic Acid Standard II (SRFA, 2S101F) was purchased from the International Humic Substances Society and used to prepare the SRFA stocks in ultrapure water. The SRFA stocks were filtered through 0.22-μm membrane filters and the concentrations of dissolved organic carbon (DOC) were quantified using a total organic carbon (TOC) analyzer (multi N/C3100, Analytik Jena AG, Jena, Germany). Natural ligands, 5 mg-C/L SRFA or 100 μM GSH, were added into a 0.1 M $NaNO_3$ solution (filtered to <0.1 μm), followed by the addition of ionic divalent iron and mercury with different Fe/Hg molar ratios, ranging from 300/1 to 1/30. These experimental matrices were then spiked with 100 μM sulfide and mixed end-over-end prior to sample characterization. The sum of the mercury and iron spikes were also kept at 100 μM. The "no ligand" controls contained the same chemical compositions except that no ligands (i.e., no SRFA or GSH) were added to these samples. The pH of all samples was adjusted to 7.0 ± 0.7 using 1 M NaOH and 1 M HNO_3. All precipitation experiments were performed inside an anaerobic chamber filled with 97% N_2 and 3% H_2 (Type A glovebox, Coy Laboratory Products Inc., USA). The initial solutions' composition and saturation indices (SI) with respect to iron sulfide (FeS) and mercury sulfide (HgS) were calculated using Visual MINTEQ 3.1.

2.2. Microbial mercury methylation experiments

The model strain of methylating bacterium, *Pseudodesulfovibrio mercurii* ND132 (*P. mercurii* ND132, previously known as *Desulfovibrio desulfuricans* ND132, Gilmour et al., 2011; Gilmour et al., 2021), was utilized for assessing the methylation potential of the Hg–S–Fe co-precipitation products. According to previously established protocols (Gilmour et al., 2011), the bacterial cultures were maintained in sulfate-reducing media and transferred to fermentative media (with sulfate replaced by fumarate as the electron acceptor) before the methylation experiments. The sulfate-free fermentative media were used to minimize the production of sulfide, which is known to influence Hg speciation and methylation. The precipitation products were synthesized as described above. Then, aliquots of each Hg–S–Fe samples were added to the late-exponential-phase cultures with equal total mercury addition of 10 nM. A separate set of aliquots from the precipitation products were centrifuged in 3 kDa ultrafiltration tubes (Amicon Ultra-4, Merck Millipore Ltd., Ireland) at 7,500 *g* for 40 min and the dissolved mercury concentrations were measured from the filtrates by following USEPA method 1631 (U.S. Environmental Protection Agency, 2002). All experiments were performed in an anaerobic chamber at room temperature (23–26 °C). Four control groups were included: (1) "abiotic control" consisting of uninoculated media amended with the precipitation products of HgS with SRFA or GSH; (2) "killed control" consisting of autoclaved cultures amended with the precipitation products of HgS with SRFA or GSH; (3) "no mercury" control consisting of active cultures amended with the precipitation products of FeS with SRFA or GSH; (4) "no iron" control consisting of active cultures amended with the precipitation products of HgS with SRFA or GSH. At each time point, triplicate cultures were sacrificed and aliquots were taken for quantification of cell density using flow cytometry (Accuri C6 Plus, BD Biosciences, USA). The bacterial cells were counted after stained with SYBR Green I (Thermo Fisher Scientific, USA). The remaining cultures were collected to quantify the concentrations of total mercury and MeHg by following USEPA method 1631 (U.S. Environmental Protection Agency, 2002) and 1630 (U.S. Environmental Protection Agency, 2001), respectively. After the mercury exposure, a subset of test cultures ($4.3 \pm 0.2 \times 10^8$ cells mL^{-1}) was centrifuged at 11,139 *g* for 5 min to collect bacterial cells, which was then resuspended in a fixative solution containing 2.5% (v/v) glutaraldehyde. Afterward, the cells were thoroughly washed with phosphate buffered saline (pH 7.4), treated with 1% osmium tetroxide, and embedded in epoxy resin. The 200–300 nm resin sections were deposited on a copper grid and examined with transmission electron

microscopy coupled with energy dispersive X-ray spectroscopy (TEM–EDX).

2.3. Characterization of Hg–S–Fe co-precipitation products

The particle morphology and chemical composition was characterized using TEM–EDX analysis (JEM-2800, JEOL Ltd., Japan). A small sample aliquot was deposited on a copper grid supported by ultrathin carbon films and allowed to air-dry prior to TEM–EDX analysis. The crystal structure of the co-precipitation products of Hg–S–Fe in the absence of thiol ligands was determined with synchrotron-based X-ray diffraction (XRD, λ = 0.68879 Å) at beamline BL14B1 of Shanghai Synchrotron Radiation Facility (SSRF). Before XRD analysis, particles were collected with filtration and freeze-drying. Immediately after addition of sulfide, the samples were mixed end over end. A 1-mL aliquot was dispensed into a cuvette and was placed in the instrument sample holder. The scattered light intensity at 90° was assessed. The hydrodynamic diameters of the precipitation products were estimated every 2 min from independent measurements consisting of ten 10-second runs on a Zetasizer instrument (Nano ZS90, Malvern Instruments Ltd., UK).

The binding environment of mercury in the precipitation products was assessed using Hg L_{III}-edge extended X-ray absorption fine structure (EXAFS) analysis at beamline BL14W1 of SSRF. We employed the solid phase extraction method reported previously to pre-concentrate our samples for Hg L_{III}-edge (12,284 eV) EXAFS analysis (Gerbig et al., 2011; Pham et al., 2014). Briefly, 1-L Hg–S–Fe samples were prepared with 5 mg-C/L SRFA, aged for up to 12 h and passed through cartridges that contained 0.4 g of C18 resins (pre-processed according to Pham et al., 2014). Afterwards, the resins were collected, homogenized with an agate mortar and pestle, loaded on an aluminum sample holder. The resins were then pressed into 10-mm slices, sealed with Kapton tapes, flash-frozen and kept in liquid N_2 prior to EXAFS analysis. Metacinnabar (β-HgS) reference material was prepared following the same procedure except that no iron or SRFA was added to the sample matrix. The mercury L_{III}-edge EXAFS spectra were collected at beamline BL14W1 of SSRF. Energy calibration was carried out using an Au foil. The electron beam energy was 3.5 GeV and the mean stored current was 200 mA. The energy of X-ray was detuned by using a fixed-exit double-crystal Si(111) monochromator. The EXAFS spectrum of the metacinnabar reference material was recorded in transmission mode using ionization chambers. For samples with low mercury content, the EXAFS spectra were collected in florescence mode using a 32-element pixel high purity Ge solid-state detector. All samples were kept under liquid N_2 atmosphere (−150 °C) during analysis. The EXAFS data were processed using ATHENA and ARTEMIS interfaces to IFEFFIT software (Newville, 2001; Ravel and Newville, 2005). After data deglitching, merging and normalization, background subtraction was performed for all sample spectra. EXAFS oscillations, $\chi(k)$, were extracted from the normalized spectra, and Fourier transformation was carried out over a k range of 2–10 $Å^{-1}$ from k-space to R-space using k^3 weighting. Our EXAFS analysis was limited to the first coordination shell. The short-range structural parameters that were determined during spectra fitting included coordination number (CN), amplitude reduction factor (S_0^2), Hg–S interatomic distances (R), Debye–Waller (DW) factors (σ^2), and energy shifts (ΔE_0). Amplitude reduction factor was fixed at 0.76 in accordance with the spectrum fitting of the metacinnabar reference material. The EXAFS signals were fitted with the ARTEMIS program (Newville, 2001; Ravel and Newville, 2005), using nonlinear least-squares curve fitting, and the precision of data fitting was estimated according to the square root of the average square difference between the fitted and measured values. We coupled different spectra of the same group during ARTEMIS running. The spectra fitting was deemed reliable as the number of variables was significantly lower than the number of independent points from the experiments. The reduced chi-square was 7 for samples formed in the presence of SRFA and the obtained R-factor was below 5.0%.

Synchrotron-based small-angle X-ray scattering (SAXS) analysis was conducted at beamline BL16B1 of SSRF to examine the time-dependent particle formation. All SAXS measurements were performed at room temperature with a three-slit collimation system at beamline BL16B1 of SSRF. After the addition of $NaNO_3$, SRFA, $FeSO_4$ and $Hg(NO_3)_2$, sulfide was added to the experimental matrices, which were immediately mixed end-over-end and injected into 1-mm sample cells sealed with Kapton tapes. The sample cells were then loaded onto a holder at a sample-to-detector distance of 1600 mm to record 2D SAXS patterns with a Pilatus 2 M area detector that collected light intensities every 2 min. The 2D SAXS patterns were converted into SAXS scattering curves with the software Fit2D from European Synchrotron Radiation Facility (Hammersley et al., 1996). The SAXS spectrum of the sample matrix containing $NaNO_3$, SRFA, $FeSO_4$ and Hg $(NO_3)_2$, but no Na_2S, was utilized for background subtraction in data analysis. After background subtraction, Lorentz-corrected intensity curves (i.e., $I \times q^2$ versus q) were plotted and used for calculating the X-ray scattering invariant (Q), which represents the total volume of particles in solution (Li et al., 1992):

$$Q = \int_0^\infty I(q) q^2 \mathrm{d}q \tag{1}$$

The extent of interactions between particulate Hg–S–Fe and SRFA was characterized using fluorescence spectroscopy. Fluorescence intensity of SRFA before and after reacting with nanoparticles was used to investigate fluorescence quenching. A 1-mL aliquot was dispensed into a quartz sample pool and placed in the sample holder for measurements. Fluorescence intensity was measured on a fluorescence spectrophotometer (F-7100, Hitachi, Japan) at a scan rate of 12000 nm/min, with sampling intervals of 5 nm for both excitation (Ex, 250–450 nm) and emission (Em, 360–540 nm) modes.

2.4. Density functional theory (DFT) calculations

The specific binding of thiol groups (represented by thioglycolic acid) on the surface of particulate Hg–S–Fe was simulated and compared to that with HgS using theoretical computation based on DFT. The geometry optimizations of HgS and Fe-incorporated HgS surfaces and their adsorptions of the thiol functional group were calculated in the DFT framework with the projector-augmented wave method in the Vienna *Ab initio* Simulation Package (VASP) (Kresse and Hafner, 1993; Kresse and Furthmuller, 1996). To describe the exchange–correlation interaction, the generalized gradient approximation with Perdew-Burke-Ernzerhof functional was utilized herein (Perdew et al., 1996). The long-range dispersion forces were accounted for employing the DFT-D3 method proposed by Grimme (Grimme et al., 2010; Grimme et al., 2011). To optimize the simulation accuracy, the Brillouin zone was sampled using a 7 × 7 × 7 Monkhorst-Pack k-points mesh for HgS bulk calculations, respectively, with a plane-wave energy cutoff of 400 eV. The atomic positions were relaxed until the Hellmann–Feynman forces on all atoms were below 0.02 eV/Å and their energy convergence of the energy difference was below 10^{-4} eV between two consecutive self-consistent steps. To mimic realistic surfaces, we constructed slab models with reasonable thickness. Specifically, for the metacinnabar (111) surface calculations, the $p(2 \times 2)$ supercell with six-layer atoms was applied and its bottom pseudo-surface atoms were passivated by pseudo-H atoms with 0.5e charge. For the (220) surface, the p

(3 × 2) supercell with four-layer atoms was applied. During the structure relaxations, both bottom Hg-S layers were fixed, while the remaining slab and the adsorbates were allowed to relax. The vacuum thickness is more than 15 Å perpendicular to the slab surface, which helps avoid artificial interaction due to periodicity. The surface energy (γ_s) for the slab model was calculated with the formula:

$$\gamma_s = \frac{1}{2A}\left(E_s^{\text{unrelaxed}} - NE_b\right) + \frac{1}{A}\left(E_s^{\text{relaxed}} - E_s^{\text{unrelaxed}}\right) \quad (2)$$

where A is the area of the surface considered, E_s^{relaxed} and $E_s^{\text{unrelaxed}}$ are the energies of the relaxed and unrelaxed surface, respectively, N is the number of atoms in the slab and E_b is the bulk energy per atom. The formation energies (E_{form}) for Fe incorporation were calculated by the following formula:

$$E_{\text{form}} = E_{\text{in}} - E_{\text{pri}} + E_{\text{Hg}} - E_{\text{Fe}} \quad (3)$$

where E_{in} and E_{pri} are the energies of the Fe incorporation and the pristine systems, E_{Hg} and E_{Fe} represent the calculated total energy of one Hg atom and one Fe atom, respectively. The adsorption energies (E_{ads}) were calculated using the equation:

$$E_{\text{ads}} = E_{\text{total}} - E_{\text{slab}} - E_{\text{adsorbate}} \quad (4)$$

where E_{total} is the energy of surface-adsorbate adsorption system, E_{slab} and $E_{\text{adsorbate}}$ is the energy of clean surface slab and free adsorbate, respectively. The charge density differences of the stable configurations with a thioglycolic acid adsorbed on surface were obtained by subtracting the charge density of the isolated surface slab and the free adsorbate from that of the surface with a thioglycolic acid adsorbed. The isosurface value is set to 0.005 e/bohr^3. The charge density differences of Fe incorporation on metacinnabar were calculated by subtracting the charge density of Fe-incorporated HgS from that of pristine HgS. The isosurface value is set to 0.05 e/bohr^3. The charge distribution of Hg and S atoms at the surface and Fe atom at the sub-surface for HgS and Fe-incorporated HgS were calculated using the Bader charge method (Bader, 1990; Henkelman et al., 2006), which split the charge density in the region between two atoms along a plane that is perpendicular to the connecting line between the two atoms. The Bader charge in positive values indicates electron deficiency. The d band center (ε_d) was computed as the first moment of the projected d band density of states. It was expressed as:

$$\varepsilon_d = \frac{\int_{-\infty}^{+\infty} n_d(\varepsilon)\varepsilon d\varepsilon}{\int_{-\infty}^{+\infty} n_d(\varepsilon) d\varepsilon} \quad (5)$$

where $n_d(\varepsilon)$ represents the density of states, and ε is the energy of states.

2.5. Statistical analyses

Statistical differences were analyzed with the one-way analysis of variance (ANOVA) for comparisons of test groups using Statistical Product and Service Solutions (SPSS, software in version 16.0). P values less than 0.05 ($p < 0.05$) were considered statistically significant.

3. Results

3.1. Mercury methylation in the presence of ferrous iron

Methylating bacteria, *P. mercurii* ND132, were exposed to the products of the anaerobic co-precipitation processes of ionic divalent mercury, sulfide and iron in the presence of SRFA or GSH, with a fixed mercury level and varied iron concentrations. The microbial MeHg production followed an unsymmetrical U-shaped trend with respect to the initial Fe/Hg molar ratios, and reached the minimal level at the Fe/Hg ratio of 1/3 (Fig. 1A–B). Compared to MeHg production in the absence of iron (i.e., "no iron" groups), the presence of ferrous iron at an initial Fe/Hg ratio of 1/3 suppressed microbial MeHg production by 90–96% (Fig. 1A–B). MeHg production was then increased by 4.6- and 3.3-fold upon further iron addition to reach Fe/Hg ratios of 3/1 and 30/1, respectively (Fig. 1A–B). The detected MeHg production was primarily originated from biomethylation of the precipitation products of Hg–S–Fe by the active cultures of *P. mercurii* ND132, as indicated by the minimal mercury background in the "no mercury" groups (Fig. S1) and negligible MeHg concentrations in the "abiotic control" and "killed control" groups (Fig. 1A–B). Bacterial growth, quantified by cell density, was indistinguishable among all the test and active control groups during the methylation experiments (Fig. S2), suggesting that the varied MeHg production was predominately due to differences in bioavailability of the mercury species formed at different iron levels.

3.2. Hg–S–Fe precursors for microbial MeHg production

TEM analysis of culture thin-sections (Fig. 1C–E) showed that nano-scale particles containing Hg, S and Fe appeared to associate with *P. mercurii* ND132 cells. Indeed, the precipitation products in the Hg–S–Fe system were nano-scale spherical particles with average diameters of 4–5 nm (Fig. 2; Fig. S4). The presence of iron and natural ligands did not apparently change the morphology or size of particle monomers (Fig. 2; Fig. S4). The three elements, namely Hg, S and Fe, were co-present in the precipitation products, as shown by the EDX spectra (Fig. 2; Fig. S4). Ultrafiltration-based mercury fractionation analysis showed that dissolved mercury remained below 0.16 ± 0.01% of total mercury addition, which further confirmed that the dominant mercury species exposed to the methylating bacteria were in particulate phase (Fig. S3).

According to the synchrotron-based XRD patterns, the dominant crystalline phase of these nanoparticles transitioned from metacinnabar to mackinawite as the initial Fe/Hg molar ratio increased from 1/30 to 300/1 (Fig. 3). The XRD spectra of the iron-rich samples showed evident diffraction patterns of mackinawite, particularly the (001) crystallographic face, and no peak shifting was observed (Fig. 3). These mackinawite particles may serve as mercury sinks as reported in previous literature (Jeong et al., 2010). For the samples precipitated at Fe/Hg ratio ranging from 1/30 to 30/1, the XRD peaks corresponding to the (111) and (220) crystallographic faces of metacinnabar gradually shifted to larger Bragg angle (θ) with increasing iron level (Fig. 3). Based on the Bragg's law (Bragg, 1913), $2d\sin\theta = n\lambda$, at a fixed incident wavelength (λ), larger Bragg angle (θ) indicates smaller interplanar spacing (d). Given the smaller ionic radius of iron relative to mercury, the XRD peak shifting indicated iron incorporation into the crystalline structure of metacinnabar. In fact, the rate-limiting step of metal sulfide nucleation is the exchange between water molecules in metal sulfide outer-sphere complexes and the inner-sphere complexes (Rickard and Luther, 2007), and the water exchange rate for mercury is orders of magnitude greater than that for ferrous iron (Morse and Luther, 1999). Therefore, prior to the formation of FeS clusters, HgS clusters are expected to form with dissolved iron incorporated into precursor structures. This is consistent with previous observations that naturally-occurring metacinnabar tended to contain iron impurities (Boctor et al., 1987), and that other "fast metals" (e.g., Cu) formed sulfide minerals more rapidly than ferrous iron and thus incorporated iron into mineral precursors during co-precipitation (Mansor et al., 2019).

Considering the indistinguishable particle sizes among all samples (Fig. 2; Fig. S4), the coordination number was fixed at 4.0 as in

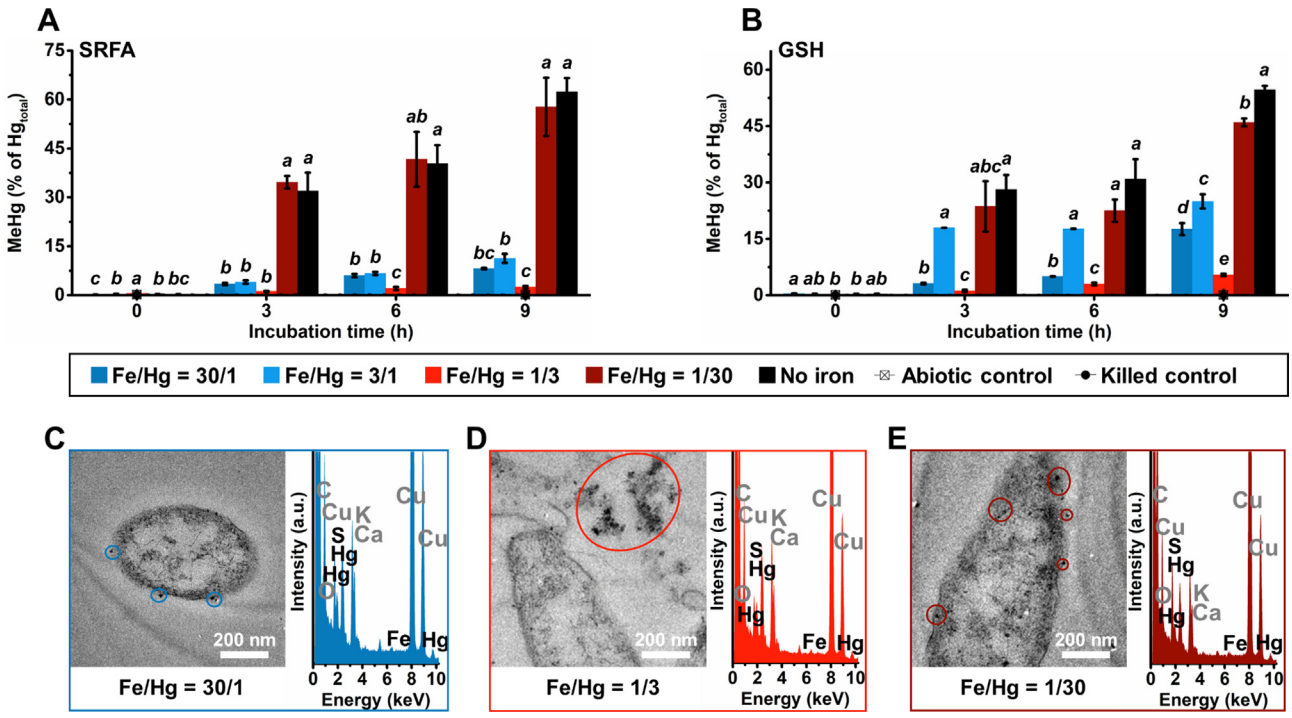

Fig. 1. Methylation potential of Hg–S–Fe co-precipitation products with natural ligands is significantly affected by Fe/Hg ratio. MeHg production from cultures of *P. mercurii* ND132 after exposure to the co-precipitation products of Hg–S–Fe formed in the presence of SRFA (**A**) and glutathione (**B**) at different initial Fe/Hg molar ratios. The concentrations of MeHg were normalized to the total concentrations of added inorganic mercury (Hg_{total}, Fig. S1). In the "no iron" control, "abiotic control" and "killed control", the precipitation products of HgS with natural ligands were added to active cultures, uninoculated media and autoclaved cultures, respectively. Error bars represent ± 1 standard deviation of triplicate samples. Values that are statistically different ($p < 0.05$) between different treatments according to the one-way ANOVA are indicated by italic lowercase letters (**A**–**B**). TEM images and EDX spectra of the thin sections of *P. mercurii* ND132 after exposed to the Hg–S–Fe co-precipitation products formed in the presence of SRFA and at initial Fe/Hg molar ratios of 30/1 (**C**), 1/3 (**D**), and 1/30 (**E**).

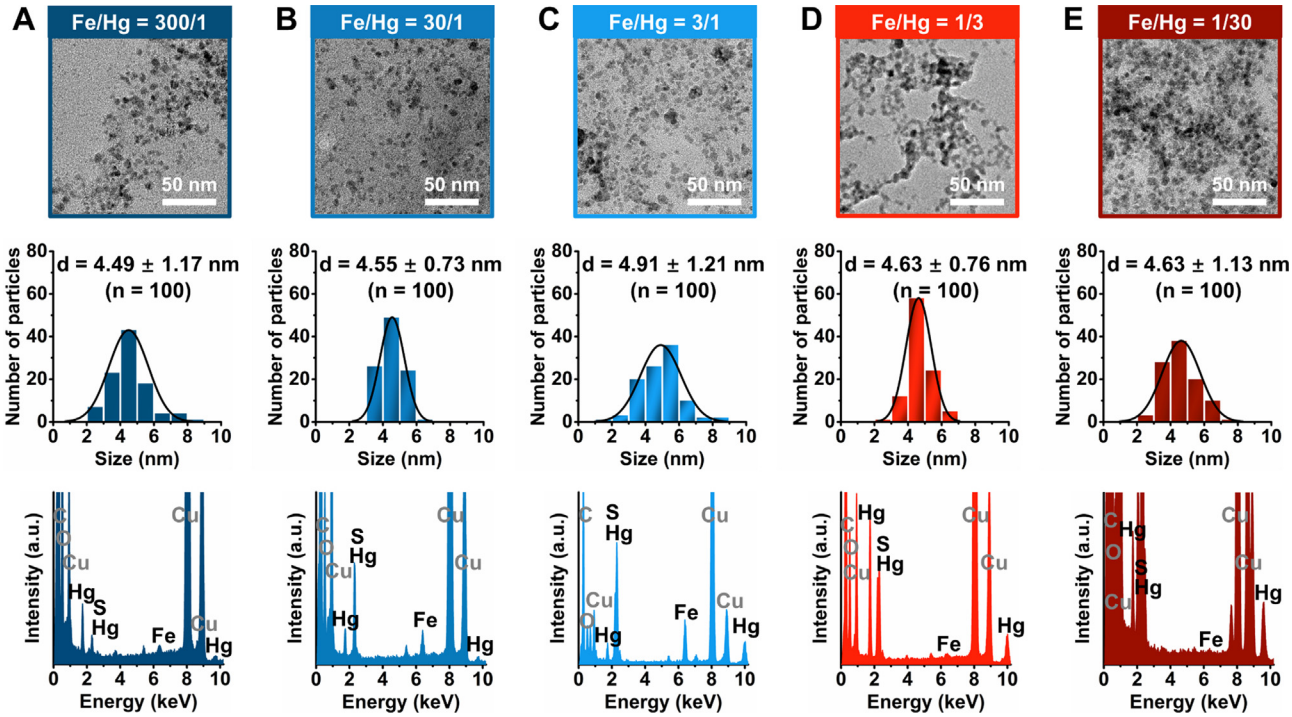

Fig. 2. Co-precipitation products of Hg–S–Fe with natural ligands at different Fe/Hg ratios are nano-scale particles with similar size and morphology. TEM images, particle size distribution, and EDX spectra of Hg–S–Fe co-precipitation products formed in the presence of SRFA at initial Fe/Hg molar ratios of 300/1 (**A**), 30/1 (**B**), 3/1 (**C**), 1/3 (**D**) and 1/30 (**E**). Particle size distribution was estimated from 100 nanoparticles observed by TEM in each sample.

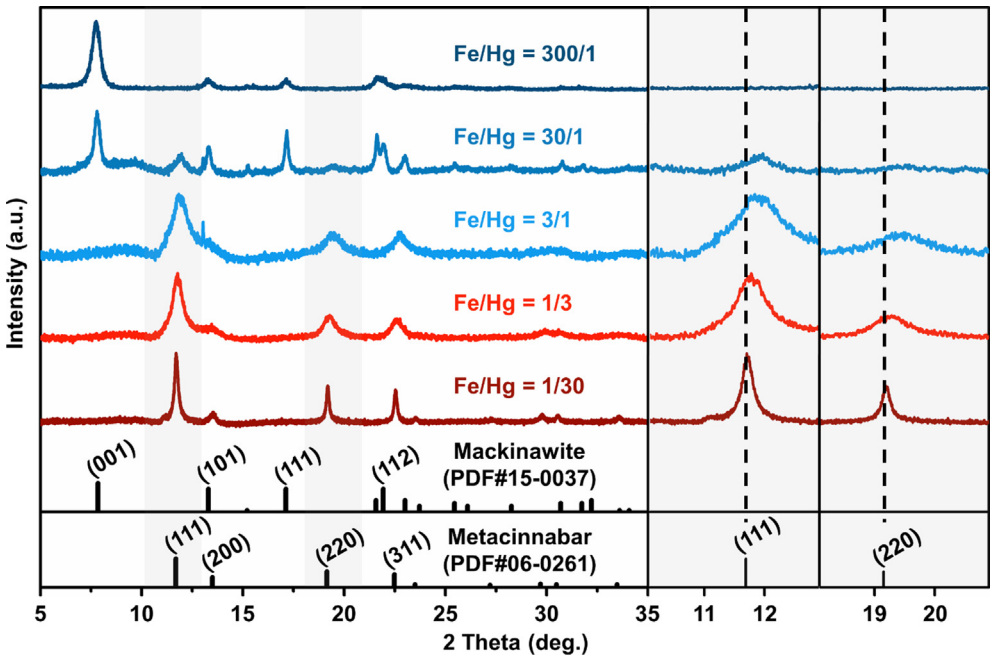

Fig. 3. Iron incorporation into crystalline structure of metacinnabar occurs during co-precipitation of Hg–S–Fe. Synchrotron-based XRD patterns (λ = 0.68879 Å) of the co-precipitation products of Hg–S–Fe at different initial Fe/Hg molar ratios. The XRD spectra within the Bragg angle range of 10.1°–12.9° and 18.1°–20.9°, containing peaks conrresponding to metacinnabar (111) and (220) facets, respectively, were enlarged and presented right to the full spectra.

the first coordination shell of metacinnabar for the EXAFS spectra fitting (Frenkel et al., 2001; Pham et al., 2014). The Hg–S interatomic distances estimated from the Hg–S–Fe samples were comparable to the metacinnabar reference material (Table S1; Fig. S5) and metacinnabar nanoparticles previously reports in the literature (Slowey, 2010; Gerbig et al., 2011; Pham et al., 2014; Poulin et al., 2017), further confirming metacinnabar was the primary mercury species in the precipitation products. The Hg–S–Fe nanoparticles formed in the presence of SRFA showed larger values of the DW factors than the metacinnabar reference material (Table S1; Fig. S5), suggesting that short-range structural disorder occurred in iron-incorporated metacinnabar nanoparticles formed with natural ligands. This observation is in line with the local structural disorder of HgS induced by NOM–HgS binding (Gerbig et al., 2011; Pham et al., 2014; Poulin et al., 2017), which, at least in part, enabled the bioavailablity of nanoparticulate metacinnabar for microbial methylation in previous research (Graham et al., 2012; Pham et al., 2014).

3.3. Aggregation status of Hg–S–Fe nanoparticles

Natural thiol ligands, including SRFA and GSH, remarkably stabilized the aggregation of nanoparticles, particularly at low Fe/Hg ratios (Fig. 4A–B). For instance, the hydrodynamic diameters of the co-precipitation products formed at Fe/Hg ratio of 1/30 were stable at 63.2 ± 12.2 nm and 75.0 ± 6.8 nm in the presence of SRFA and GSH, respectively (Fig. 4A–B). The co-precipitation products formed at the same Fe/Hg ratio without ligands exhibited drastically increasing hydrodynamic diameters, i.e., going beyond 800 nm immediately after data collection (Fig. 4C). In the absence of thiol ligands, larger aggregates of nanoparticles occurred during precipitation of HgS and Hg–S–Fe at lower Fe/Hg ratios (Fig. 4C). More interestingly, the co-precipitation products formed at the initial Fe/Hg ratio of 1/3 strongly aggregated whether thiol ligands were present or not (Fig. 4). Taken together, our data revealed that Hg–S–Fe nanoparticles formed aggregates in aquatic environment and this process was significantly susceptible to the presence of natural thiol ligands and the relative abundance of iron versus mercury. Further fluorescence analysis and theoretical calculations demonstrated that the effects of iron on the formation of nanoparticle aggregates occurred through modifying the chemical binding strength between thiol groups and surface mercury atoms (Figs. 5–6).

4. Discussion

4.1. Methylation potential of iron-incorporated nano-metacinnabar correlates inversely with nanoparticle aggregation

Iron-incorporated metacinnabar nanoparticles agglomerated to form particle aggregates, and the aggregation state of these nanoparticles (Fig. 4) appeared to dictate their methylation potential (Fig. 1). In the cultures exhibiting relatively high MeHg production, Hg–S–Fe nanoparticles scattered around bacterial cells (Fig. 1C and 1E), whereas highly aggregated Hg–S–Fe nanoparticles (>350 nm) were detected from the bacterial samples that produced minimal level of MeHg at the initial Fe/Hg ratio of 1/3 (Fig. 1D). At this Fe/Hg ratio, Hg–S–Fe precipitation products strongly aggregated regardless of whether natural ligands were present (Fig. 4). Considering the important role of interfacial processes on cell surface in dictating mercury uptake and methylation (Schaefer et al., 2011; Schaefer et al., 2014; Lu et al., 2018), the severe aggregation of nanoparticulate mercury likely limited the available particle surfaces for interacting with methylating bacterial cells and led to the substantially mitigated MeHg production.

The observation of total particle volume assessed using SAXS analysis remaining nearly constant (Fig. S6) while the hydrodynamic diameter of Hg–S–Fe precipitation products apparently increasing with time (Fig. 4) suggests that the formation of Hg–S–Fe nanoparticle aggregates occurred through a rapid initial nucleation step followed by a relatively slow reorganization of the already formed particles (e.g., oriented attachment) (Bolze et al., 2004; Teng, 2013; De Yoreo et al., 2015). The presence of ferrous iron modulated nanoparticle aggregation by affecting both

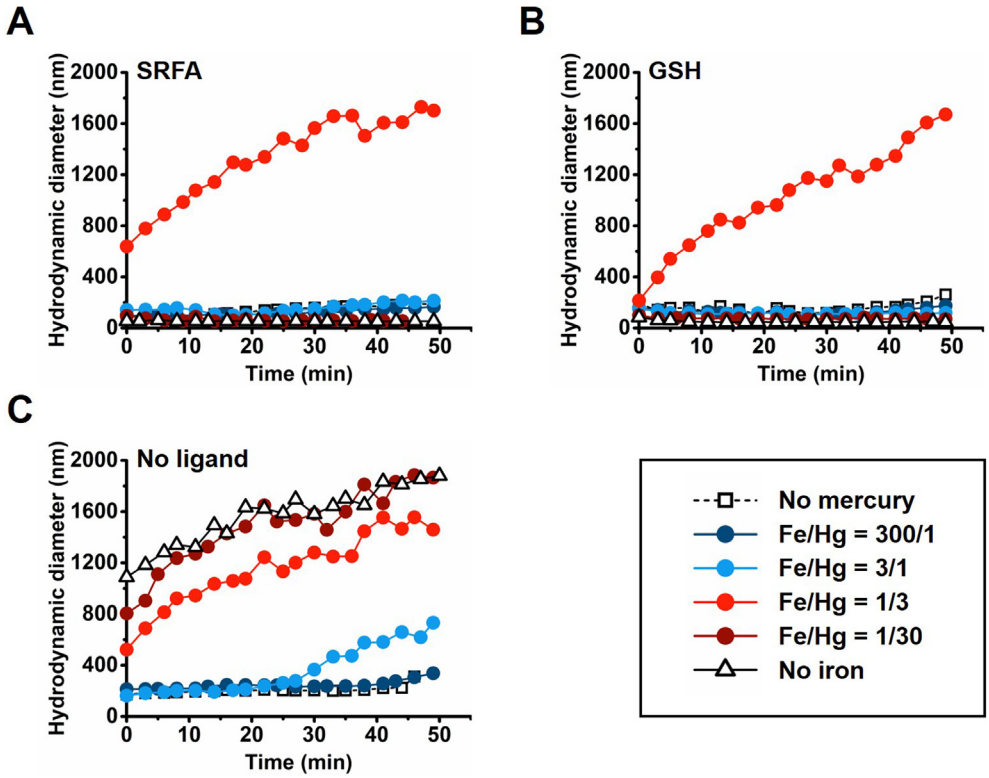

Fig. 4. Aggregation state of Hg–S–Fe nanoparticles is significantly affected by natural ligands and Fe/Hg ratio. Time-dependent hydrodynamic diameter measurements of the co-precipitation products of Hg–S–Fe formed in the presence of SRFA (**A**) or glutathione (**B**) and in the absence of ligand (**C**) at different initial Fe/Hg molar ratios assessed using dynamic light scattering.

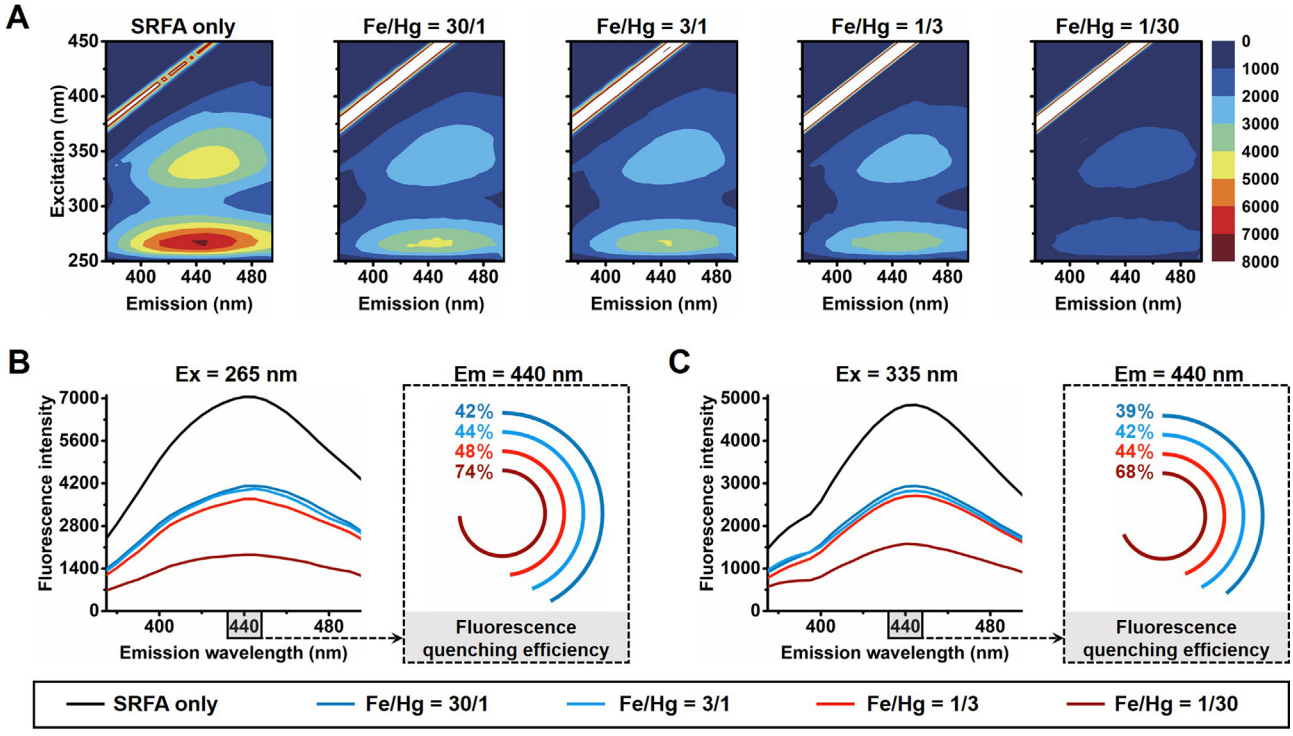

Fig. 5. Chemical binding between Hg–S–Fe nanoparticles and natural ligands is mitigated as Fe/Hg ratio increases. Three-dimensional excitation–emission matrix (3D-EEM) fluorescence spectra (**A**) of SRFA before and after interacting with Hg–S–Fe co-precipitation products formed at different initial Fe/Hg molar ratios. Fluorescence quenching at excitation wavelengths of 265 nm (**B**) and 335 nm (**C**) induced by interactions of Hg–S–Fe with SRFA at different initial Fe/Hg molar ratios. The fluorescence quenching efficiencies were calculated at Ex/Em of 265/440 nm (**B**) and 335/440 nm (**C**), respectively.

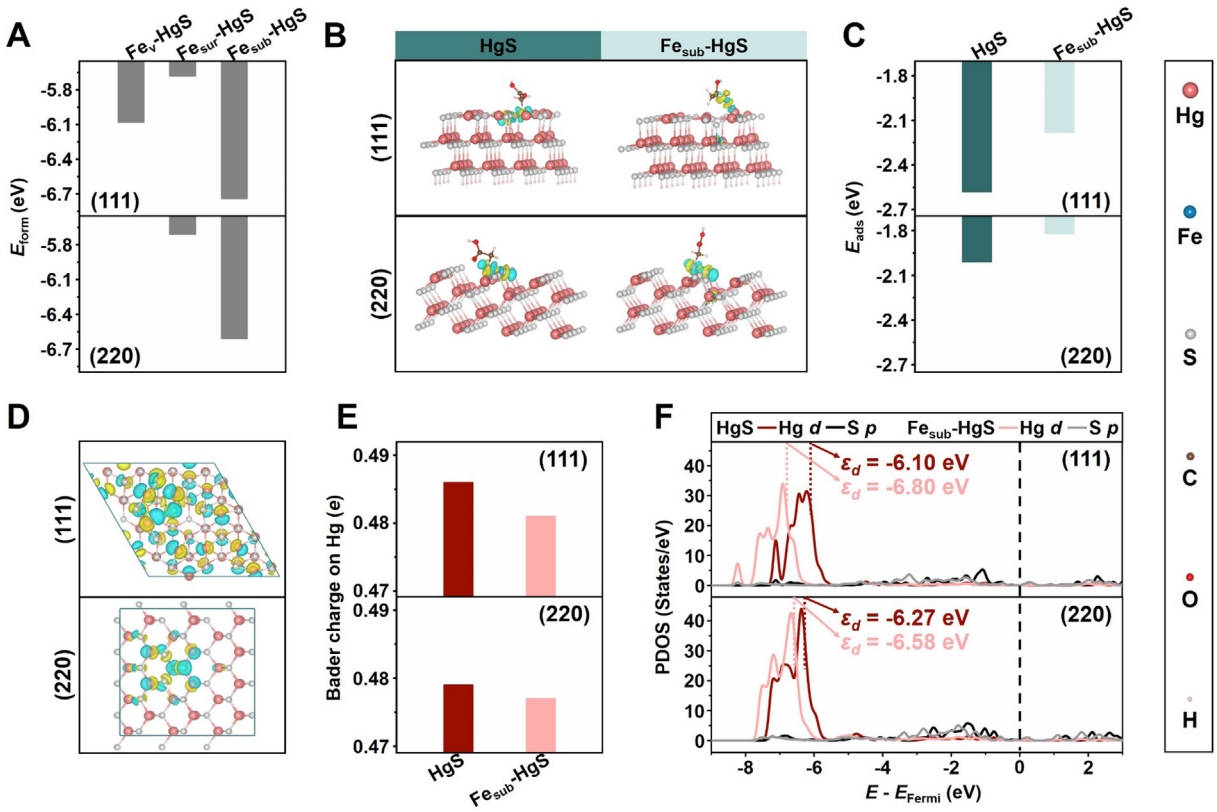

Fig. 6. Sub-surface iron incorporation weakens chemical binding between metacinnabar facets and thiol ligands. The calculated formation energies of metacinnabar (111) or (220) facet with Fe incorporation (**A**). The preferable adsorption configurations of thioglycolic acid on metacinnabar (111) or (220) facet with or without Fe incorporation (**B**) and the corresponding adsorption energies (**C**). The plots of charge density difference on metacinnabar (111) or (220) facet induced by Fe incorporation (**D**), the Bader charge of the interacting surface Hg atoms (**E**), and the PDOS projected on the interacting surface Hg *d*-states and S *p*-states and calculated Hg *d* band center (ε_d) (**F**). The yellow and cyan regions in (**B**) and (**D**) indicate charge density increase and decrease, respectively. HgS refers to the pristine metacinnabar facet, Fe_v-HgS refers to the facet with Hg vacancy embedded by Fe atom, and Fe_{sur}-HgS and Fe_{sub}-HgS refer to the facet with Hg atom in the surface and sub-surface layer substituted by Fe atom, respectively. (For interpretation of the references to colour in this figure legend, the reader is referred to the web version of this article.)

nucleation and particle attachment in the opposite directions, particularly when natural ligands were present, and thus led to the non-monotonical trend of the nano-aggregate size with respect to the initial Fe/Hg ratio (Fig. 4A–B). In fact, the total particle volume substantially decreased with the increasing iron level (Fig. S6), probably because large relative Fe/Hg abundance mitigated nucleation by reducing the supersaturation level of sparingly soluble mineral metacinnabar (Table S2). As a result, formation of large nano-aggregates was lessened by the smaller probability of particle–particle collision due to the lower density of particle monomers (Fig. 4C). Moreover, the growth of nanoparticle aggregates at low Fe/Hg ratios, was stabilized by natural ligands (Fig. 4A–B), likely attributable to the inhibitory effects of capping agents on the orientated attachment of nanoparticle monomers via physical separations, such as steric hindrance and electrostatic repulsion (Deonarine and Hsu-Kim, 2009; De Yoreo et al., 2015). Nanoparticle–ligand binding was previously proven essential for stabilizing metal sulfide nanoparticles (Deonarine and Hsu-Kim, 2009), and structural incorporation of iron may interfere with nanoparticle–ligand binding through changing the surface charge distribution of metacinnabar.

4.2. Iron incorporation enhances nano-metacinnabar aggregation by weakening mercury–thiol binding

Fluorescence quenching experiments were carried out to elucidate the effects of iron incorporation on the interactions between nano-metacinnabar and natural ligands. The fluorescence spectra of SRFA displayed a primary peak at excitation/emission wavelengths (Ex/Em) of 260–270/435–450 nm and a secondary peak at Ex/Em of 325–355/420–470 nm (Fig. 5A), which corresponded to fulvic acid-like and humic acid-like materials, respectively (Chen et al., 2003). SRFA appeared to chemically bind with nanoparticulate mercury via these fluorescent components, as suggested by the strong quenching of the corresponding fluorescence peaks (Fig. 5). The extent of SRFA–nanoparticle binding decreased with the increasing iron level, in that, the fluorescence intensities of SRFA were quenched by 74%, 48%, 44% and 42% at 265/440 nm (Fig. 5B) and by 68%, 44%, 42% and 39% at 335/440 nm (Fig. 5C), when the initial Fe/Hg molar ratio rose from 1/30 to 1/3, 3/1 and 30/1 for co-precipitation, respectively. At the Fe/Hg ratio of 1/3, nanoparticle–ligand binding was evidently weakened due to iron incorporation (Fig. 5), whereas precipitation occurred at a relatively high extent (Fig. S6). Thus, the incorporation of ferrous iron lessened the effect of natural ligands in hindering aggregation of nanoparticulate Hg–S–Fe under these conditions and highly aggregated nanoparticles occurred (Figs. 1D, 4A, 4B).

Numerous studies have shown that naturally-occurring ligands (e.g., NOM, peptides) bind with soft-metal containing nanoparticles mainly through thiol complexation (Gerbig et al., 2011; Qi et al., 2020). Hence, we utilized DFT computational methods to simulate the interactions between thiol moieties (using thioglycolic acid as a model compound) and the surficial layers of nanoparticulate mercury to understand the influence of iron incorporation on ligand binding. The surface models of metacinnabar (111) and (220) were established for theoretical calculations, as these facets are relatively stable with low surface energy (Table S3) and iron incorporation occurred to both facets upon

Hg–S–Fe co-precipitation (Fig. 3). Metacinnabar (111) facet with Hg-vacancy defects is more structurally stable than the intact counterpart due to the surface unsaturated dangling bonds (Fig. S7), analogous to the previously reported atomic arrangements of sphalerite (111) facet (Wright et al., 1998). According to the calculated formation energies, the incorporated Fe atoms tend to substitute the sub-surface Hg atoms of both facets rather than substitute the surface Hg atoms or embed the Hg vacancies on (111) facet (Fig. 6A; Fig. S7).

The nature of the binding between nano-metacinnabar and thiol ligands is mainly chemisorption, as reflected by the significant charge transfer occurring between the thiol moieties and the metacinnabar facets (Fig. 6B). This chemical binding is compromised upon iron incorporation according to the less negative adsorption energies (Fig. 6C). Indeed, the surface charge distribution is apparently modified on both (111) and (220) (Fig. 6D) and the Bader charges of the surface Hg atoms become less positive (Fig. 6E), when the sub-surface Hg atoms are substituted by Fe atoms. Moreover, the projected density of states (PDOS) show that the *d* band centers (ε_d) of surface Hg atoms shift away from the Fermi energy level upon sub-surface iron incorporation, corresponding to lower potential of metal–ligand charge transfer (Fig. 6F). Taken together, iron incorporation into the sub-surface of metacinnabar leads to charge re-distribution on both (111) and (220), and subsequently decreases the tendency of surface Hg atoms to accept lone pairs of electrons from thiols to form inner-sphere coordination bonds.

4.3. Implications for metal biogeochemistry

Co-occurrence of mercury, ferrous iron, sulfide and natural ligands is commonly encountered by mercury-methylating microorganisms in natural aquatic environments. Iron concentrations may be orders of magnitude higher than the mercury concentrations in pristine environments, with the Fe/Hg ratio as large as 3000000/1 (Bone et al., 2014). In such environment, iron sulfides predominantly form and serve as adsorbents for mercury and control bioavailability of mercury (Skyllberg and Drott, 2010; Skyllberg et al., 2021). Yet, the mercury abundance tends to be high and the Fe/Hg ratio is generally below 300/1 in Hg-impacted areas, such as paddy soils and sediments affected by mining activities or chemical industrial wastes (Merritt and Amirbahman, 2007; Rothenberg and Feng, 2012; Fathi et al., 2013; Barringer et al., 2013; Vlassopoulos et al., 2018). These scenarios likely lead to co-precipitation of ferrous iron, mercury and sulfide, and subsequently intensive microbial MeHg production, with iron-incorporated nanoparticulate metacinnabar being the main precursor for microbial MeHg production. Iron amendments for minimizing mercury bioavailability and the risks of *in situ* MeHg formation should aim to achieve a system-specific Fe/Hg ratio that maximizes Hg–S–Fe nanoparticle aggregation and limits interfacial reactions with methylating bacteria. This ideal Fe/Hg ratio may vary with environmental conditions that determine the abundance of ionic mercury, ferrous iron and sulfide, such as metal-complexing ligands, pH and redox potential. In addition to the degree of saturation, special attention may focus on the ligand-rich macromolecules that modulate the short-range structure and aggregation of nanoparticles via inner-sphere coordination with mercury.

Considering that the water exchange rates of other soft metals (e.g., Zn, Cu, Pb, Cd) were substantially greater than that of ferrous iron, these nano-scale metal sulfides are expected to form with iron incorporations during co-precipitation processes with ubiquitous ferrous iron and soft ligands (Hochella et al., 2005; Mansor et al., 2019). These processes may be particularly intensified by the evolving natural conditions and human activities, such as thawing of the permafrost (Klaminder et al., 2010; St Pierre et al., 2018; Schaefer et al., 2020) and the rise of deep-sea mining (Koschinsky et al., 2001; Paul et al., 2021). Furthermore, iron doping is a widely used method for enhancing specific functions, such as the photocatalytic and magnetic properties, of engineered metal sulfide nanomaterials (Saha et al., 2017). Hence, metal sulfide nanoparticles originated from both natural and anthropogenic sources likely contain iron impurities, and an important implication from our research is that the structure and bioavailability (as toxins or nutrients) of these nano-scale materials may not be accurately predicted according to their iron-free counterparts. The effects of iron incorporation on the environmental behavior and impact of nano-scale metal sulfides ought to be evaluated and may follow nonmonotonic (e.g., U-shaped) trends as a function of iron abundance.

Declaration of Competing Interest

The authors declare that they have no known competing financial interests or personal relationships that could have appeared to influence the work reported in this paper.

Acknowledgements

This work was supported by the National Natural Science Foundation of China (22125603, 21976095, 22020102004), Tianjin Municipal Science and Technology Commission (21JCJQJC00060, 20JCZDJC00690) and Ministry of Education of China (T2017002). We thank Cynthia C. Gilmour for supplying *Pseudodesulfovibrio mercurii* ND132, Zhiying Zhang for assisting with SAXS analysis, and beamlines BL14W1, BL16B1 and BL14B1 of Shanghai Synchrotron Radiation Facility for providing the beam time.

Appendix A. Supplementary material

Data Availability: Research Data associated with this article can be accessed at https://doi.org/10.17605/OSF.IO/6ACGZ. Supplementary material to this article can be found online at https://doi.org/10.1016/j.gca.2023.03.035.

References

Bader, R.F.W., 1990. Atoms in Molecules: A Quantum Theory. Oxford Univ Press, New York.
Barringer, J.L., Szabo, Z., Reilly, P.A., Riskin, M.L., 2013. Variable contributions of mercury from groundwater to a first-order urban Coastal Plain stream in New Jersey, USA. Water Air Soil Pollut. 224 (4), 1475.
Benoit, J.M., Gilmour, C.C., Mason, R.P., Heyes, A., 1999. Sulfide controls on mercury speciation and bioavailability to methylating bacteria in sediment pore waters. Environ. Sci. Technol. 33 (6), 951–957.
Boctor, N.Z., Shieh, Y.N., Kullerud, G., 1987. Mercury ores from the New Idria Mining District, California: Geochemical and stable isotope studies. Geochim. Cosmochim. Acta 51 (6), 1705–1715.
Bolze, J., Pontoni, D., Ballauff, M., Narayanan, T., Colfen, H., 2004. Time-resolved SAXS study of the effect of a double hydrophilic block-copolymer on the formation of $CaCO_3$ from a supersaturated salt solution. J. Colloid Interf. Sci. 277 (1), 84–94.
Bone, S.E., Bargar, J.R., Sposito, G., 2014. Mackinawite (FeS) reduces mercury(II) under sulfidic conditions. Environ. Sci. Technol. 48 (18), 10681–10689.
Bragg, W.L., 1913. The diffraction of short electromagnetic waves by a crystal. Proc. Cambridge Philos. Soc. 17, 43–57.
Bravo, A.G., Bouchet, S., Guedron, S., Amouroux, D., Dominik, J., Zopfi, J., 2015. High methylmercury production under ferruginous conditions in sediments impacted by sewage treatment plant discharges. Water Res. 80, 245–255.
Chen, W., Westerhoff, P., Leenheer, J.A., Booksh, K., 2003. Fluorescence excitation−emission matrix regional integration to quantify spectra for dissolved organic matter. Environ. Sci. Technol. 37 (24), 5701–5710.
Cossa, D., Garnier, C., Buscail, R., Elbaz-Poulichet, F., Mikac, N., Patel-Sorrentino, N., Tessier, E., Rigaud, S., Lenoble, V., Gobeil, C., 2014. A Michaelis-Menten type equation for describing methylmercury dependence on inorganic mercury in aquatic sediments. Biogeochemistry 119 (1–3), 35–43.
De Yoreo, J.J., Gilbert, P.U.P.A., Sommerdijk, N.A.J.M., Penn, P.R.L., Whitelam, S., Joester, D., Zhang, H.Z., Rimer, J.D., Navrotsky, A., Banfield, J.F., Wallace, A.F.,

Michel, Meldrum, F.C., Colfen, H., Dove, P.M., 2015. Crystallization by particle attachment in synthetic, biogenic, and geologic environments. Science 349 (6247), aaa6760.
Deonarine, A., Hsu-Kim, H., 2009. Precipitation of mercuric sulfide nanoparticles in NOM-containing water: Implications for the natural environment. Environ. Sci. Technol. 43 (7), 2368–2373.
Driscoll, C.T., Mason, R.P., Chan, H.M., Jacob, D.J., Pirrone, N., 2013. Mercury as a global pollutant: Sources, pathways, and effects. Environ. Sci. Technol. 47 (10), 4967–4983.
Fathi, M., Ridal, J.J., Lean, D.R.S., Blais, J.M., 2013. Do wood fibers from a pulp mill affect the distribution of total and methyl mercury in river sediments? J. Great Lakes Res. 39 (1), 66–73.
Frenkel, A.I., Hills, C.W., Nuzzo, R.G., 2001. A view from the inside: Complexity in the atomic scale ordering of supported metal nanoparticles. J. Phys. Chem. B 105 (51), 12689–12703.
Gerbig, C.A., Kim, C.S., Stegemeier, J.P., Ryan, J.N., Aiken, G.R., 2011. Formation of nanocolloidal metacinnabar in mercury-DOM-Sulfide systems. Environ. Sci. Technol. 45 (21), 9180–9187.
Gilmour, C.C., Elias, D.A., Kucken, A.M., Brown, S.D., Palumbo, A.V., Schadt, C.W., Wall, J.D., 2011. Sulfate-reducing bacterium *Desulfovibrio desulfuricans* ND132 as a model for understanding bacterial mercury methylation. Appl. Environ. Microbiol. 77 (12), 3938–3951.
Gilmour, C.C., Bell, J.T., Soren, A.B., Riedel, G., Riedel, G., Kopec, A.D., Bodaly, R.A., 2018. Distribution and biogeochemical controls on net methylmercury production in Penobscot River marshes and sediment. Sci. Total Environ. 640, 555–569.
Gilmour, C.C., Soren, A.B., Gionfriddo, C.M., Podar, M., Wall, J.D., Brown, S.D., Michener, J.K., Urriza, M.S.G., Elias, D.A., 2021. *Pseudodesulfovibrio mercurii* sp. nov., a mercury-methylating bacterium isolated from sediment. Int. J. Syst. Evol. Microbiol. 71 (3), 004697.
Graham, A.M., Aiken, G.R., Gilmour, C.C., 2012. Dissolved organic matter enhances microbial mercury methylation under sulfidic conditions. Environ. Sci. Technol. 46 (5), 2715–2723.
Graham, A.M., Aiken, G.R., Gilmour, C.C., 2013. Effect of dissolved organic matter source and character on microbial Hg methylation in Hg–S–DOM solutions. Environ. Sci. Technol. 47 (11), 5746–5754.
Grimme, S., Antony, J., Ehrlich, S., Krieg, H., 2010. A consistent and accurate *ab initio* parametrization of density functional dispersion correction (DFT-D) for the 94 elements H-Pu. J. Chem. Phys. 132 (15), 154104.
Grimme, S., Ehrlich, S., Goerigk, L., 2011. Effect of the damping function in dispersion corrected density functional theory. J. Comput. Chem. 32 (7), 1456–1465.
Hammersley, A.P., Svensson, S.O., Hanfland, M., Fitch, A.N., Häusermann, D., 1996. Two-dimensional detector software: From real detector to idealised image or two-theta scan. High Pressure Res. 14, 235–248.
Han, S., Obraztsova, A., Pretto, P., Deheyn, D.D., Gieskes, J., Tebo, B.M., 2008. Sulfide and iron control on mercury speciation in anoxic estuarine sediment slurries. Mar. Chem. 111 (3–4), 214–220.
Henkelman, G., Arnaldsson, A., Jonsson, H., 2006. A fast and robust algorithm for Bader decomposition of charge density. Comput. Mater. Sci. 36 (3), 354–360.
Hochella, M.F., Moore, J.N., Putnis, C.V., Putnis, A., Kasama, T., Eberl, D.D., 2005. Direct observation of heavy metal-mineral association from the Clark Fork River Superfund Complex: Implications for metal transport and bioavailability. Geochim. Cosmochim. Acta 69 (7), 1651–1663.
Jeong, H.Y., Klaue, B., Blum, J.D., Hayes, K.F., 2007. Sorption of mercuric ion by synthetic manocrystalline mackinawite (FeS). Environ. Sci. Technol. 41 (22), 7699–7705.
Jeong, H.Y., Sun, K., Hayes, K.F., 2010. Microscopic and spectroscopic characterization of Hg(II) immobilization by mackinawite (FeS). Environ. Sci. Technol. 44 (19), 7476–7483.
Jonsson, S., Skyllberg, U., Nilsson, M.B., Westlund, P.O., Shchukarev, A., Lundberg, E., Bjorn, E., 2012. Mercury methylation rates for geochemically relevant Hg-II species in sediments. Environ. Sci. Technol. 46 (21), 11653–11659.
Jonsson, S., Skyllberg, U., Nilsson, M.B., Lundberg, E., Andersson, A., Bjorn, E., 2014. Differentiated availability of geochemical mercury pools controls methylmercury levels in estuarine sediment and biota. Nat. Commun. 5, 4624.
Klaminder, J., Hammarlund, D., Kokfelt, U., Vonk, J.E., Bigler, C., 2010. Lead contamination of subarctic lakes and its response to reduced atmospheric fallout: Can the recovery process be counteracted by the ongoing climate change? Environ. Sci. Technol. 44 (7), 2335–2340.
Koschinsky, A., Gaye-Haake, B., Arndt, C., Maue, G., Spitzy, A., Winkler, A., Halbach, P., 2001. Experiments on the influence of sediment disturbances on the biogeochemistry of the deep-sea environment. Deep Sea Res. Part II 48 (17–18), 3629–3651.
Kresse, G., Furthmuller, J., 1996. Efficient iterative schemes for *ab initio* total-energy calculations using a plane-wave basis set. Phys. Rev. B: Condens. Matter 54 (16), 11169–11186.
Kresse, G., Hafner, J., 1993. *Ab initio* molecular dynamics for liquid metals. Phys. Rev. B: Condens. Matter 47 (1), 558–561.
Li, Y., Gao, T., Chu, B., 1992. Synchrotron SAXS studies of the phase-separation kinetics in a segmented polyurethane. Macromolecules 25 (6), 1737–1742.
Lovley, D.R., 1991. Dissimilatory Fe(III) and Mn(IV) reduction. Microbiol. Rev. 55 (2), 259–287.
Lu, X., Johs, A., Zhao, L.D., Wang, L.H., Pierce, E.M., Gu, B.H., 2018. Nanomolar copper enhances mercury methylation by *Desulfovibrio desulfuricans* ND132. Environ. Sci. Technol. Lett. 5 (6), 372–376.
Mansor, M., Berti, D., Hochella Jr., M.F., Murayama, M., Xu, J., 2019. Phase, morphology, elemental composition, and formation mechanisms of biogenic and abiogenic Fe-Cu-sulfide nanoparticles: A comparative study on their occurrences under anoxic conditions. Am. Mineral. 104 (5), 703–717.
Mazrui, N.M., Jonsson, S., Thota, S., Zhao, J., Mason, R.P., 2016. Enhanced availability of mercury bound to dissolved organic matter for methylation in marine sediments. Geochim. Cosmochim. Acta 194, 153–162.
Mazrui, N.M., Seelen, E., King'ondu, C.K., Thota, S., Awino, J., Rouge, J., Zhao, J., Mason, R.P., 2018. The precipitation, growth and stability of mercury sulfide nanoparticles formed in the presence of marine dissolved organic matter. Environ. Sci.-Proc. Imp. 20 (4), 642–656.
Mehrotra, A.S., Horne, A.J., Sedlak, D.L., 2003. Reduction of net mercury methylation by iron in *Desulfobulbus propionicus* (1pr3) cultures: Implications for engineered wetlands. Environ. Sci. Technol. 37 (13), 3018–3023.
Mehrotra, A.S., Sedlak, D.L., 2005. Decrease in net mercury methylation rates following iron amendment to anoxic wetland sediment slurries. Environ. Sci. Technol. 39 (8), 2564–2570.
Merritt, K.A., Amirbahman, A., 2007. Mercury dynamics in sulfide-rich sediments: Geochemical influence on contaminant mobilization within the Penobscot River estuary, Maine, USA. Geochim. Cosmochim. Acta 71 (4), 929–941.
Morse, J.W., Luther, G.W., 1999. Chemical influences on trace metal-sulfide interactions in anoxic sediments. Geochim. Cosmochim. Acta 63 (19–20), 3373–3378.
Muyzer, G., Stams, A.J.M., 2008. The ecology and biotechnology of sulphate-reducing bacteria. Nat. Rev. Microbiol. 6 (6), 441–454.
Ndu, U., Christensen, G.A., Rivera Jr., N.A., Gionfriddo, C.M., Deshusses, M.A., Elias, D. A., Hsu-Kim, H., 2018. Quantification of mercury bioavailability for methylation using diffusive gradient in thin-film samplers. Environ. Sci. Technol. 52 (15), 8521–8529.
Newville, M., 2001. EXAFS analysis using FEFF and FEFFIT. J. Synchrotron Radiat. 8, 96–100.
Parks, J.M., Johs, A., Podar, M., Bridou, R., Jr, H.R.A., Smith, S.D., Tomanicek, S.J., Qian, Y., Brown, S.D., Brandt, C.C., Palumbo, A.V., Smith, J.C., Wall, J.D., Elias, D.A., Liang, L.Y., 2013. The genetic basis for bacterial mercury methylation. Science 339 (6125), 1332–1335.
Paul, S.A.L., Zitoun, R., Noowong, A., Manirajah, M., Koschinsky, A., 2021. Copper-binding ligands in deep-sea pore waters of the Pacific Ocean and potential impacts of polymetallic nodule mining on the copper cycle. Sci. Rep. 11 (1), 18425.
Perdew, J.P., Burke, K., Ernzerhof, M., 1996. Generalized gradient approximation made simple. Phys. Rev. Lett. 77 (18), 3865–3868.
Pham, A.L.T., Morris, A., Zhang, T., Ticknor, J., Levard, C., Hsu-Kim, H., 2014. Precipitation of nanoscale mercuric sulfides in the presence of natural organic matter: Structural properties, aggregation, and biotransformation. Geochim. Cosmochim. Acta 133, 204–215.
Podar, M., Gilmour, C.C., Brandt, C.C., Soren, A., Brown, S.D., Crable, B.R., Palumbo, A. V., Somenahally, A.C., Elias, D.A., 2015. Global prevalence and distribution of genes and microorganisms involved in mercury methylation. Sci. Adv. 1 (9), e1500675.
Poulin, B.A., Aiken, G.R., Nagy, K.L., Manceau, A., Krabbenhoft, D.P., Ryan, J.N., 2016. Mercury transformation and release differs with depth and time in a contaminated riparian soil during simulated flooding. Geochim. Cosmochim. Acta 176, 118–138.
Poulin, B.A., Gerbig, C.A., Kim, C.S., Stegemeier, J.P., Ryan, J.N., Aiken, G.R., 2017. Effects of sulfide concentration and dissolved organic matter characteristics on the structure of nanocolloidal metacinnabar. Environ. Sci. Technol. 51 (22), 13133–13142.
Qi, Y., Zhang, T., Jing, C.Y., Liu, S.J., Zhang, C.D., Alvarez, P.J.J., Chen, W., 2020. Nanocrystal facet modulation to enhance transferrin binding and cellular delivery. Nat. Commun. 11 (1), 1262.
Ravel, B., Newville, M., 2005. ATHENA, ARTEMIS, HEPHAESTUS: data analysis for X-ray absorption spectroscopy using IFEFFIT. J. Synchrotron Radiat. 12, 537–541.
Rickard, D., Luther, G.W., 2007. Chemistry of iron sulfides. Chem. Rev. 107 (2), 514–562.
Rivera Jr., N.A., Bippus, P.M., Hsu-Kim, H., 2019. Relative reactivity and bioavailability of mercury sorbed to or coprecipitated with aged iron sulfides. Environ. Sci. Technol. 53 (13), 7391–7399.
Rothenberg, S.E., Feng, X.B., 2012. Mercury cycling in a flooded rice paddy. J. Geophys. Res. 117, G03003.
Saha, A., Makkar, M., Shetty, A., Gahlot, K., Pavan, A.R., Viswanatha, R., 2017. Diffusion doping in quantum dots: bond strength and diffusivity. Nanoscale 9 (8), 2806–2813.
Schaefer, K., Elshorbany, Y., Jafarov, E., Schuster, P.F., Striegl, R.G., Wickland, K.P., Sunderland, E.M., 2020. Potential impacts of mercury released from thawing permafrost. Nat. Commun. 11 (1), 4650.
Schaefer, J.K., Rocks, S.S., Zheng, W., Liang, L.Y., Gu, B.H., Morel, F.M.M., 2011. Active transport, substrate specificity, and methylation of Hg(II) in anaerobic bacteria. Proc. Natl. Acad. Sci. U. S. A. 108 (21), 8714–8719.
Schaefer, J.K., Szczuka, A., Morel, F.M.M., 2014. Effect of divalent metals on Hg (II) uptake and methylation by bacteria. Environ. Sci. Technol. 48 (5), 3007–3013.
Skyllberg, U., Drott, A., 2010. Competition between disordered iron sulfide and natural organic matter associated thiols for mercury(II)-An EXAFS study. Environ. Sci. Technol. 44 (4), 1254–1259.

Skyllberg, U., Persson, A., Tjerngren, I., Kronberg, R.M., Drott, A., Meili, M., Bjorn, E., 2021. Chemical speciation of mercury, sulfur and iron in a dystrophic boreal lake sediment, as controlled by the formation of mackinawite and framboidal pyrite. Geochim. Cosmochim. Acta 294, 106–125.

Slowey, A.J., 2010. Rate of formation and dissolution of mercury sulfide nanoparticles: The dual role of natural organic matter. Geochim. Cosmochim. Acta 74 (16), 4693–4708.

St Pierre, K.A., Zolkos, S., Shakil, S., Tank, S.E., St. Louis, V.L., Kokelj, S.V., 2018. Unprecedented increases in total and methyl mercury concentrations downstream of retrogressive thaw slumps in the western Canadian Arctic. Environ. Sci. Technol. 52 (24), 14099–14109.

Tang, W.L., Liu, Y.R., Guan, W.Y., Zhong, H., Qu, X.M., Zhang, T., 2020. Understanding mercury methylation in the changing environment: Recent advances in assessing microbial methylators and mercury bioavailability. Sci. Total Environ. 714, 136827.

Teng, H.H., 2013. How ions and molecules organize to form crystals. Elements 9 (3), 189–194.

Tian, L., Guan, W.Y., Ji, Y.Y., He, X., Chen, W., Alvarez, P.J.J., Zhang, T., 2021. Microbial methylation potential of mercury sulfide particles dictated by surface structure. Nat. Geosci. 14 (6), 409–416.

U.S. Environmental Protection Agency, 2001. Method 1630: Methyl Mercury in Water by Distillation, Aqueous Ethylation, Purge and Trap, and CVAFS. Washington, DC: U.S. Environmental Protection Agency.

U.S. Environmental Protection Agency, 2002. Method 1631, Revision E: Mercury in Water by Oxidation, Purge and Trap, and Cold Vapor Atomic Fluorescence Spectroscopy. Washington, DC: U.S. Environmental Protection Agency.

Ulrich, P.D., Sedlak, D.L., 2010. Impact of iron amendment on net methylmercury export from tidal wetland microcosms. Environ. Sci. Technol. 44 (19), 7659–7665.

United Nations Environment Programme, 2019. *Global Mercury Assessment 2018.* Geneva, Switzerland: United Nations Environment Programme, Chemicals and Health Branch.

Vlassopoulos, D., Kanematsu, M., Henry, E.A., Goin, J., Leven, A., Glaser, D., Brown, S. S., O'Day, P.A., 2018. Manganese(IV) oxide amendments reduce methylmercury concentrations in sediment porewater. Environ. Sci.-Proc. Imp. 20 (12), 1746–1760.

Wright, K., Watson, G.W., Parker, S.C., Vaughan, D.J., 1998. Simulation of the structure and stability of sphalerite (ZnS) surfaces. Am. Mineral. 83 (1–2), 141–146.

Xu, J., Bland, G.D., Gu, Y., Ziaei, H., Xiao, X.Y., Deonarine, A., Reible, D., Bireta, P., Hoelen, T.P., Lowry, G.V., 2021. Impacts of sediment particle grain size and mercury speciation on mercury bioavailability potential. Environ. Sci. Technol. 55 (18), 12393–12402.

Zhang, T., Kim, B., Leyard, C., Reinsch, B.C., Lowry, G.V., Deshusses, M.A., Hsu-Kim, H., 2012. Methylation of mercury by bacteria exposed to dissolved, nanoparticulate, and microparticulate mercuric sulfides. Environ. Sci. Technol. 46 (13), 6950–6958.

Zhang, T., Kucharzyk, K.H., Kim, B., Deshusses, M.A., Hsu-Kim, H., 2014. Net methylation of mercury in estuarine sediment microcosms amended with dissolved, nanoparticulate, and microparticulate mercuric sulfides. Environ. Sci. Technol. 48 (16), 9133–9141.